Acta Materialia 222 (2022) 117424

Contents lists available at ScienceDirect

Acta Materialia

journal homepage: www.elsevier.com/locate/actamat

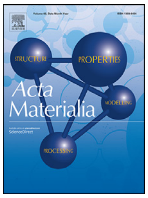

Full length article

Evolution of length scales and of chemical heterogeneity during primary and secondary dealloying

Yong Li[a,b], Bao-Nam Ngo-Dinh[b,c], Jürgen Markmann[a,b], Jörg Weissmüller[a,b,*]

[a] *Institute of Materials Physics and Technology, Hamburg University of Technology, Hamburg, Germany*
[b] *Institute of Materials Mechanics, Helmholtz-Zentrum Hereon, Geesthacht, Germany*
[c] *Institute for Materials, Technical University of Braunschweig, Braunschweig, Germany*

ARTICLE INFO

Article history:
Received 2 August 2021
Revised 15 October 2021
Accepted 16 October 2021
Available online 25 October 2021

Keywords:
Nanoporous gold
Dealloying
Alloy corrosion
Kinetic monte carlo simulation

ABSTRACT

We study the evolution of silver-rich regions, or ‘clusters’, during the making of nanoporous gold by dealloying. The clusters, which are remnants of the master alloy that have evaded corrosion, impact the functional behavior of the material. Furthermore, they carry information on the structure size in the initial stages of dealloying. Using kinetic Monte Carlo simulations, we emulate electrochemical dealloying at various electrode potentials. Our simulations illustrate the two-stage character of the process, where primary dealloying generates the initial network of nanoscale ligaments, while the subsequent secondary dealloying is characterized by coarsening and further dissolution. Silver-rich clusters, embedded in essentially pure gold, form during primary dealloying throughout the range of dealloying potentials of the study. At this point, their size scales with that of the ligaments. Both sizes decrease with increasing dealloying potential, and the trends of size versus potential agree with a Gibbs-Thompson type relation. Yet, when coarsening increases the ligament size during secondary dealloying, the size of the silver clusters remains constant. Directly accessing the initial ligament size of nanoporous gold in experiment is challenging, yet our study links this size to that of the silver-rich clusters. The clusters survive even in the later stages of dealloying and their size can be measured. This provides an experimental signature of the initial size.

1. Introduction

Dealloyed nanoporous metals, and specifically nanoporous gold (NPG), are of interest as functional material for actuators [1–5], catalysts [6–8], sensors [9–11], and energy storage [12–14]. As bicontinuous networks of nanoscale ligaments, they also offer opportunities for fundamental studies of the mechanics, thermodynamics, and kinetics [15–18] at the nanoscale.

The nanoscale network of NPG is the product of a corrosion process in which the less noble constituent Ag is dissolved from its solid solution with the more noble constituent, Au. As a general rule, NPG retains some of the initial Ag. The residual Ag atom fraction, $x_{\mathrm{Ag}}^{\mathrm{res}}$, varies from 0.60 down to 0.02 [19,20]. The impact of residual Ag on Young’s modulus [21] and strength [22] of NPG have been reported. Residual Ag also reinforces the surface-enhanced Raman scattering (SERS) of NPG [23]. When NPG serves as a heterogeneous catalyst, increasing $x_{\mathrm{Ag}}^{\mathrm{res}}$ can enhance the reactivity, as has been found for CO oxidation [24,25], or it can severely impair it, as for the example of methanol oxidation [26,27]. Finally, achieving control over the residual Ag is a prerequisite for multistep dealloying protocols that have been used for creating NPG with a hierarchical nested-network nanostructure [28,29].

Typically, the spatial distribution of the residual Ag is of relevance. Catalysis, for instance, is sensitive to segregation (or not) of Ag to the surface. Multistep dealloying protocols require a homogeneous distribution of Ag in the porous material that serves as a template for a second dealloying step. These remarks motivate that detailed information on the evolution of the residual Ag content and the processes that govern the distribution of Ag within the NPG microstructure is important for understanding both, dealloying and the behavior of the dealloyed metal.

The present understanding of the atomic-scale processes behind the nanostructure formation by dealloying of Ag-Au rests largely on a study by Erlebacher using kinetic Monte-Carlo simulation [30]. Along with follow-up work by the same technique [31–34], that study establishes how the nucleation of vacancy islands – en-

---

[*] Corresponding author.
E-mail address: weissmueller@tuhh.de (J. Weissmüller).

https://doi.org/10.1016/j.actamat.2021.117424

abling the attack of lower terraces and, thereby, the growth of new pore channels – competes with the passivation that results from the surface enrichment in Au. Bifurcation at the tips of advancing pore channels creates a network of nanoscale ligaments, again covered with a nearly passivating Au layer. That layer has been imaged with atom probe tomography [35]. The passivation implies buried regions of the master alloy that are not immediately attacked by the corrosion. Yet, as the corrosion front propagates into the depth of the master alloy, the nanoscale network structure that was formed during the initial corrosion events (”primary dealloying” [19]) coarsens by surface diffusion. That process (”secondary dealloying” [19]) redistributes the Au component, thereby gradually uncovering more and more of the buried regions and promoting further dissolution of Ag.

By a combination of simulation and element-sensitive, transmission-electron-microscopy-based tomography, it has been demonstrated that remnants of the Ag-rich regions survive even after the extensive microstructural coarsening that accompanies the later stages of corrosion [33]. These regions take the form of isolated nanoscale clusters, and their local composition agrees with that of the master alloy [26,33]. Even though each Ag-rich cluster may eventually be dissolved, the Ag in the surviving ones has never been redistributed by diffusion. Annealing – without dissolution – is required for homogenizing the Ag distribution in NPG [33].

While the net Ag content decreases throughout the dealloying, the above-mentioned studies do not reveal whether and how the mean size of the discrete Ag regions evolves. The suggestion [33] that they retain their mean size awaits verification. That notion is relevant, since it implies that the clusters are representative of the initial ligament structure, which is formed as a result of the nanoscale self organization during primary dealloying. Experimental data on the initial ligament size – which is an important characteristic of dealloying – remain elusive. Many experimental studies of NPG report ligament sizes of several tens of nanometers. This appears consistent with in-situ small angle scattering studies of dealloying, which suggests initial sizes around 20–30 nm for NPG [36–38]. Yet, as coarsening concurs with dealloying, even the in situ experiments average over microstructural regions in different stages of corrosion and coarsening and so may not catch the initial ligament size in isolation. If it could be confirmed that the size of the silver clusters remains invariant during coarsening, then these microstructural features could provide a persistent signature of the ligament size during primary dealloying. They would then be a basis for investigating the initial microstructure ex situ by TEM studies even in material that has undergone substantial coarsening during secondary dealloying.

Here, we use kinetic Monte Carlo (kMC) simulation for studying the evolution of the nanostructure of NPG during primary and secondary dealloying, with an emphasis on characterizing the silver-rich clusters. We confirm that the size of those features remains invariant even after substantial ligament coarsening, and we link that size to the initial ligament size.

2. Methods

2.1. Dealloying simulations

We used an independent implementation of the kMC algorithm described in detail by Erlebacher [30], adopting also all materials parameters of that study. That approach reaches semi-quantitative agreement with experimental signatures of dealloying [30–33]. The initial structure is a random substitutional solid solution of Ag and Au on a rigid, face-centered cubic (FCC) crystal lattice. A free surface is open to corrosion, and periodic boundary conditions are assumed in the in-plane directions. Two fundamental types of events are allowed: surface diffusion of any atom, and dissolution of Ag atoms only.

In a diffusion event, an atom with nearest-neighbor coordination number n may jump to one of its vacant neighboring sites. The hopping rate, k_n^{diff}, associated with this type of event is

$$k_n^{\text{diff}} = \nu_{\text{D}} \exp \frac{nE_{\text{b}}}{k_{\text{B}}T}, \tag{1}$$

with ν_{D} the Debye frequency, E_b the bond energy, k_{B} the Boltzmann constant, and T the temperature. We took $\nu_{\text{D}} = 10^{13}$ s^{-1} and $E_b = -0.15$ eV; this is consistent with earlier work [30,33]. Also as in earlier work [33], only jumps to a target site with at least three neighbor atoms are allowed for diffusion events. This suppresses regular Schwöbel jumps. All simulations in this work were run at $T = 300$ K.

Dissolution events are also treated by a bond breaking model. Here, only Ag atoms are considered, and the activation energy is modified by a parameter, ϕ, that measures the ”dealloying potential”, more precisely, a product of the electrode potential – which drives the dissolution in a dealloying experiment – and the charge transfer per dissolved atom, here one elementary charge. With attention to dealloying above the critical dealloying potential and, hence, with a large net driving force for dissolution, the model ignores redeposition processes. The per-atom rate of dissolution events associated with n-coordinated Ag atoms is thus

$$k_n^{\text{diss}} = \nu_{\text{E}} \exp \frac{nE_{\text{b}} + \phi}{k_{\text{B}}T}. \tag{2}$$

Here, ν_{E} represents an effective attempt frequency that includes the energy barrier governing the exchange-current density. We used $\nu_{\text{E}} = 10^4$ s^{-1} [30]. Dissolution is limited to surface Ag atoms with more than 3 vacant neighboring sites.

The simulation unit cell is a rectangular parallelepiped comprising 2.1×10^6 atoms and bounded by {111}-, {110}- and {112}-type faces. The free surface for corrosion is (111)-oriented, and periodic boundary conditions apply in the orthogonal directions. With a lattice parameter of 408 pm, the thickness of the unit cell is 30.1nm and its lateral extensions are 36.8 and 31.9 nm in the $[1\bar{1}0]$ and the $[11\bar{2}]$ direction, respectively. Initially, the lattice sites are occupied at random, with a net atom fraction $\text{Ag}_{75}\text{Au}_{25}$. That composition is used in typical experimental studies of NPG.

Values of ϕ ranging from 1.00 eV to 1.25 eV were applied. This potential range gives an interval of 3×10^4 in dealloying time, which is sufficient for our analysis of the dealloying kinetics.

We used the open-source software Ovito [39] for visualization. The ”Cluster Analysis” modifier in Ovito (with the cut-off radius set to 3.0 Å, just beyond the nearest-neighbor spacing) was used for identifying and displaying percolating clusters during primary dealloying.

2.2. Analysis of characteristic size

Our analysis of characteristic length scales, L, is based on autocorrelation functions. The autocorrelation function, H, of a phase in a microstructure measures the average, over all material points in that phase, of the fraction of the phase in a spherical shell with radius r around the respective material point. The initial slope of $H(r)$ gives the reciprocal of the feature size according to [40,41]

$$L^{-1} = -\left.\frac{\mathrm{d}H}{\mathrm{d}r}\right|_{r=0}. \tag{3}$$

In this way, a mean ligament size was determined by analysis of the autocorrelation function, H_{total}, of the entire solid phase (comprising Au and Ag). Furthermore, we have computed the Ag-Ag autocorrelation function, $H_{\text{Ag-Ag}}$, based exclusively on the Ag component. This provided the basis for analyzing the mean size of the Ag

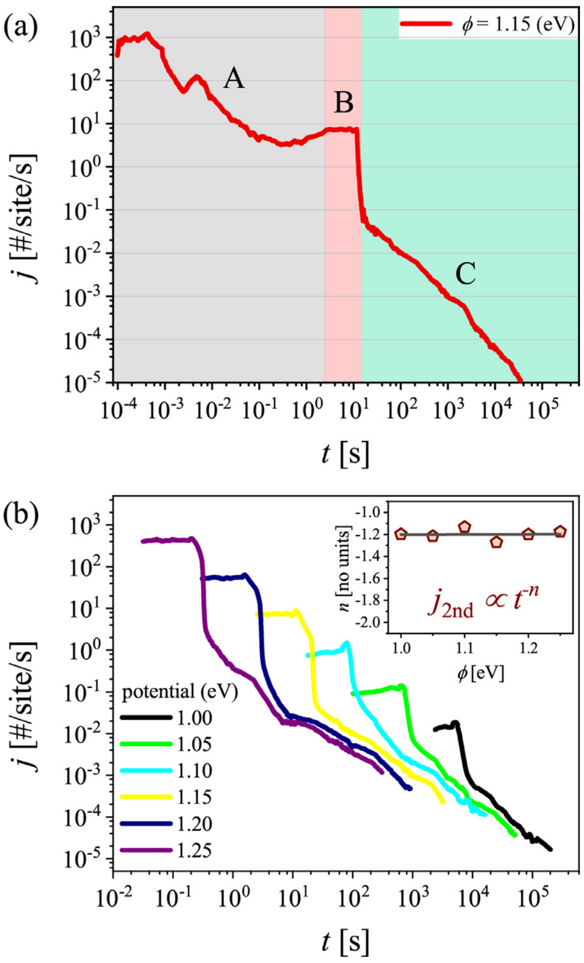

Fig. 1. Evolution of the dissolution current. (a) Log-log graph of flux density, j, as a function of dealloying time, t, at dealloying potential $\phi = 1.15$ eV. Shaded regions denote stages of initial surface layer roughening and passivation (A), steady-state dealloying front propagation (B), and coarsening of the completely porous sample (C). Note the drop in j upon transition from stage B to C. (b) Log-log graph of $j(t)$ during stages B and C for different ϕ. Inset: power law exponent n in $j \propto t^n$ versus ϕ during stage C, as obtained from linear regression to $j(t)$ on the log-log scale of the graph. Note n appears independent of ϕ, with mean value $n = 1.20 \pm 0.07$ (horizontal line in graph).

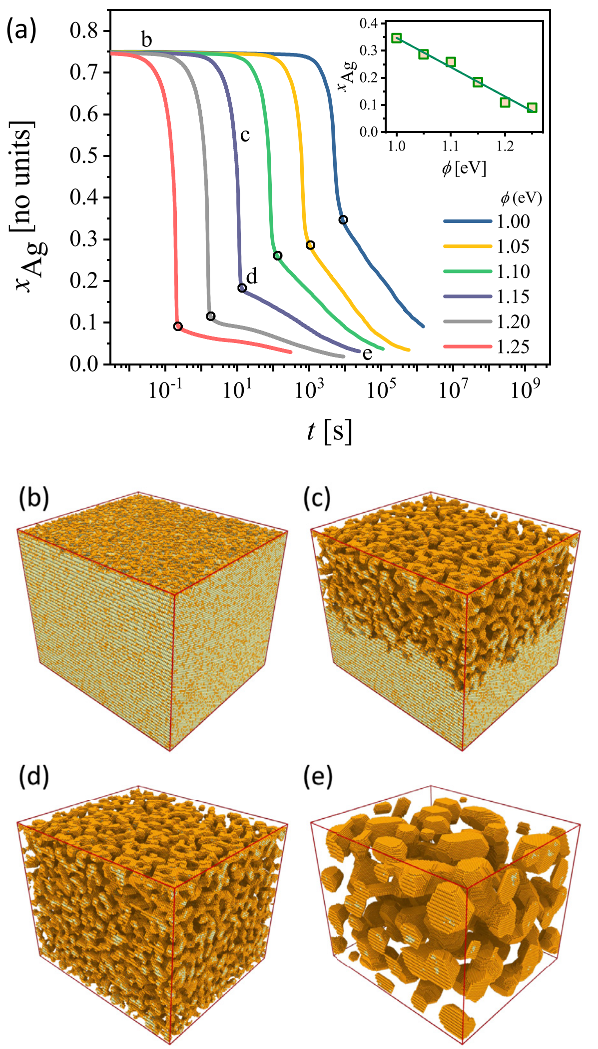

Fig. 2. Primary and secondary dealloying. (a) Ag fraction, x_{Ag}, versus dealloying time, t, during dealloying at different ϕ. Discontinuous change in slope of $x_{Ag}(t)$ marks transition (open circles) between primary and secondary dealloying. Inset: x_{Ag} at the point of transition, plotted versus ϕ. (b-d) Renderings of microstructure at different time during dealloying at $\phi = 1.15$ eV, see also markers on the respective graph in (a). Master alloy after dissolution of roughly one monolayer (b) shows initial surface roughening and partial passivation by enrichment in Au. During primary dealloying (c), corrosion front is seen to separate master alloy from nanoscale network. At the transition between primary and secondary dealloying (d), master alloy is completely consumed. Secondary dealloying (e) concurs with coarsening of the ligaments.

clusters. In each case, the periodic boundary conditions were taken into account when computing $H(r)$.

3. Results

3.1. Dissolution flux density and Ag content

We first inspect the evolution of the dissolution flux density, j, which is defined as the number of dissolved Ag atoms per site of the original master alloy surface and per time. When multiplied with the elementary charge, j represents a dissolution current density that scales with the experimental current density (per area of the macroscopic, external surface) of electrochemical dealloying experiments.

Fig. 1 a shows j versus the dealloying time, t, for the example of $\phi = 1.15$ eV. In line with Ref [30], j exhibits three apparent stages. The onset of dealloying – stage A in the figure – exhibits the very high j of a pristine alloy surface, prior to the formation of a passivating Au layer. This stage corresponds to the dissolution of the first few atomic layers only. The subsequent plateau – stage B – with essentially constant j characterizes the emergence of a steady-state dissolution front that propagates into the depth of the sample. A sharp drop of j is observed when that front has swept the entire sample. Dissolution then continues, in stage C, yet with much smaller j and at an ever decreasing rate. Note the logarithmic time axis of Fig 1a; stage A is extremely brief and stage C has by very far the longest duration.

Fig. 1 b shows analogous graphs for different dealloying potentials, omitting stage A and focussing on stages B, C for clarity. While rates increase and time scales decrease with increasing ϕ, it is seen that the same general phenomenology – and specifically the two well-separated stages – are consistently observed at any potential.

Fig. 2 a shows how the Ag atom fraction, x_{Ag}, evolves with time for different dealloying potentials. All graphs exhibit a fast initial decay that ends in a discontinuous change in slope. That change (open circles in Fig. 2a) reflects the sharp drop in j of Fig. 1b, in other words, the transition between stages B and C. The large change in dealloying rate is exemplified by the graph at $\phi = 1.15$

eV. While it takes only ~14 s for the Ag content to decrease from 0.75 to ~ 0.18, at least 2.5×10^4 s is needed for decreasing x_{Ag} by the same factor again, to reach ~0.03.

Figs. 2 b-e display the evolution of the microstructure for the example of $\phi = 1.15$ eV. It is obvious that the fast dissolution in stage B corresponds to a quasi steady state where the corrosion front propagates through the sample, while the slow dissolution in stage C concurs with coarsening.

The discontinuous change in slope of $x_{\mathrm{Ag}}(t)$ and the associated drop in the dissolution current mark the instant when the corrosion front has crossed the entire sample, in other words, the transition between primary and secondary dealloying. That observation applies at each ϕ. The finding establishes that the sharp drop in $j(t)$ and the associated change in slope of $x_{\mathrm{Ag}}(t)$ mark the transition between primary and secondary dealloying.

With the signature of the transition between primary and secondary dealloying established, Fig. 1 is seen to imply constant dissolution current and, hence, constant velocity of the corrosion front during primary dealloying at any given value of ϕ. By contrast – see inset in the figure – secondary dealloying is distinguished by a power law behavior where j decays with time according to $j \propto t^{-n}$, with the exponent $n = 1.20 \pm 0.07$, independent of ϕ.

The residual Ag fraction after primary dealloying decreases with increasing dealloying potential (Fig. 2a Inset). For example, an increase of ϕ from 1.00 eV to 1.25 eV leads to a decrease of x_{Ag} from 0.35 to 0.10 in the primary-dealloyed samples.

3.2. Composition profile and microstructure

Fig. 3 a inspects a snapshot of the microstructure during primary dealloying. The rendering at the top of the figure shows all atoms, Ag and Au, in a column along the corrosion direction, cut from the simulation unit cell. Distinct regions corresponding to the master alloy and the primary dealloyed NPG are apparent, with a transition region of finite thickness at the corrosion front. For the same subvolume of the simulation, the rendering in the centre of the figure shows the Ag atoms only. Each group of atoms forming an individual contiguous (by nearest-neighbor contacts) cluster is shown in a separate hue. The display illustrates the transition from the single percolating cluster (gray) of the master alloy to isolated clusters (colored) behind the corrosion front. Composition profiles were constructed by taking the average, $\bar{x}_{\mathrm{Ag}}$, of the Ag fraction in each of the $l = 1 \ldots 129$ layers of the entire simulation unit cell (with $l = 1$ referring to the external surface layer) parallel to the external surface and plotting $\bar{x}_{\mathrm{Ag}}$ versus l. The graph of $\bar{x}_{\mathrm{Ag}}$ versus depth at the bottom of Fig 3a shows that the Ag fraction is sensibly constant at $\bar{x}_{\mathrm{Ag}} \approx 0.18$ in the primary-dealloyed structure.

Fig. 3 b plots the composition profile of the corrosion run of Fig. 3a at different dealloying time. As above, $\bar{x}_{\mathrm{Ag}}$ is sensibly constant in the primary dealloyed NPG. It is only at the much longer times that correspond to secondary dealloying that $\bar{x}_{\mathrm{Ag}}$ can be seen to slowly and uniformly drop.

The evolution of the composition profile suggests that the dissolution of Ag behind the corrosion front is negligible in the primary dealloying stage. This is simply a consequence of the very short duration of the primary dealloying and of the much longer duration of the secondary dealloying. It is this difference in timescales that allows us to discuss the two dealloying stages separately. Hence, in the subsequent analysis, the evaluation of Ag cluster size and ligament size was done on the NPG structure part of the partially dealloyed sample at primary dealloying stage, while such an evaluation of sizes will be done for the entire structure at secondary dealloying stage.

Focusing on the secondary dealloying stage at $\phi = 1.15$ eV, Fig. 4 shows slices through the sample. Ag atoms (green) appear

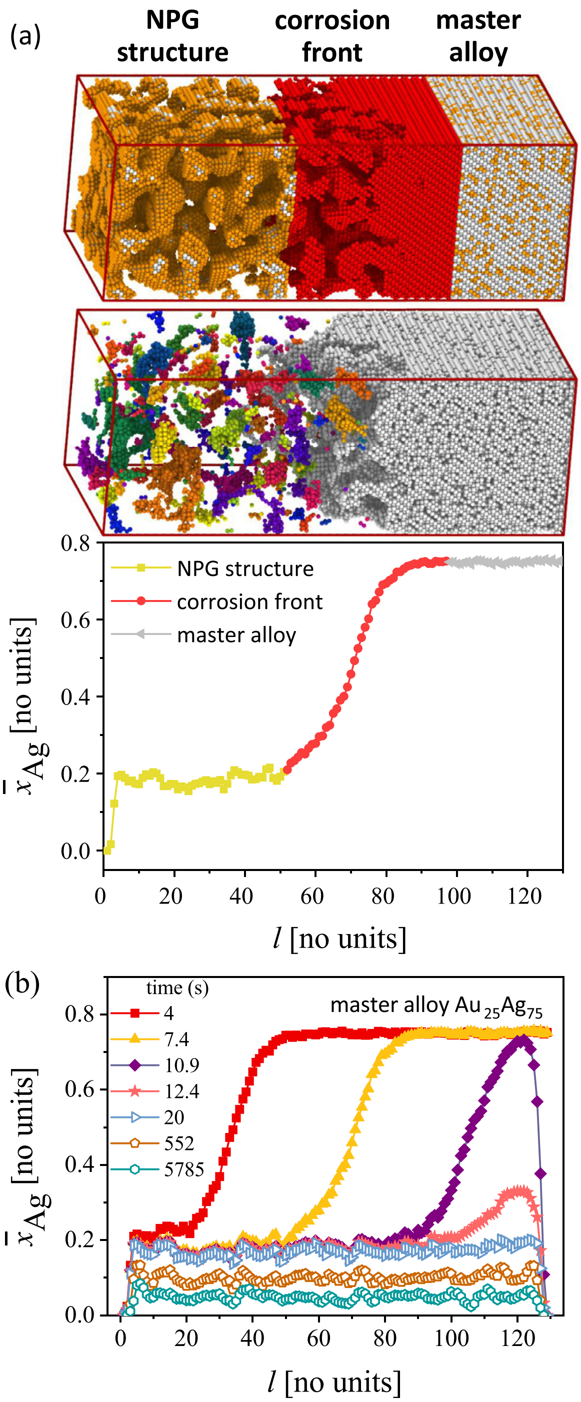

Fig. 3. Evolution of composition and formation of Ag clusters during primary dealloying. (a) Rendering (top) of all atoms in partially dealloyed structure at time $t = 7.4$ s exhibits three regions: Ligament network of primary dealloyed NPG (left), corrosion front (middle), and virgin master alloy (right). Ag and Au atoms are shown in gray and golden, respectively. Rendering (centre) of Ag atoms only in the same structure as top shows contiguous cluster in the master alloy disintegrating into isolated clusters behind the corrosion front. Each contiguous cluster of Ag atom is distinguished by an individual color. Graph (bottom) of Ag fraction, $\bar{x}_{\mathrm{Ag}}$, of each layer l in that state shows sensibly constant composition in the primary dealloyed part. (b) Composition profiles at various instants, as detailed in legend. All graphs are for dealloying at $\phi = 1.15$ eV. Ag fractions in (a) and (b) represent averages over cross-sectional planes from the entire simulation unit cell. For clarity, renderings in part (a) show only a subvolume of that cell. (For interpretation of the references to colour in this figure legend, the reader is referred to the web version of this article.)

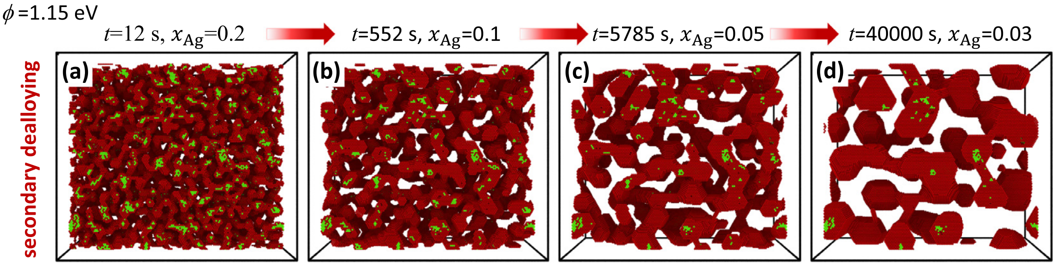

Fig. 4. Renderings of slices cutting through NPG structures at different time during secondary dealloying at $\phi = 1.15$ eV. Au and Ag atoms are coded red and green, respectively. (a-d) Secondary dealloying gradually dissolves Ag clusters and coarsen ligaments. No redistribution of Ag atoms are observed and mean silver cluster size seems to be constant. (For interpretation of the references to colour in this figure legend, the reader is referred to the web version of this article.)

aggregated in Ag-rich clusters within a matrix of pure Au (red). The initial structure in this figure corresponds to the end of primary dealloying. Here, the Ag clusters tend to extend throughout the ligaments and up to a thin (essentially one atomic layer) passivation layer of pure gold at their surface. Thus, the characteristic size, L_{Ag}, of the clusters is slightly smaller than the characteristic size, L_{lig}, of the ligaments. As ligaments coarsen during secondary dealloying, the number of Ag clusters diminishes. Yet, the characteristic size of the surviving clusters remains sensibly constant. The next section presents a quantitative analysis of the evolution of L_{Ag} and L_{lig}.

3.3. Silver cluster size and ligament size

Figs. 5 a,b plot the autocorrelation functions for all atoms, $H_{total}(r)$, and selectively for the silver component, $H_{Ag-Ag}(r)$, at different dealloying time. The implications for the evolution of L_{lig} and L_{Ag}, based on Eq 3, during dealloying are shown in Figs. 5c, along with x_{Ag}. These data yield two notable observations, which we found to apply generally to dealloying at all investigated ϕ. Firstly, both L_{Ag} and L_{lig} remain constant throughout the primary dealloying. Secondly, while L_{lig} increases during secondary dealloying, L_{Ag} remains constant.

Fig. 6 a inspects how L_{Ag} and the ligament size, L^0_{lig}, during primary dealloying vary with ϕ. It is seen that L^0_{lig} is quite sensitive to ϕ, covering a factor of 4 within the potential interval of our investigation. Furthermore, we find that the inverse of each of the characteristic sizes varies linearly with the dealloying potential. Straight lines of best fit to both data sets converge to the identical ϕ-value, $\phi = 0.900 \pm 0.002$ eV, in the limit of infinite size. This is consistent with a constant ratio between the two sizes. The slopes indicate that this ratio takes the value $L_{lig}/L_{Ag} = 1.28$. This is also borne out when size-ratios are computed individually at each ϕ, as indicated by the inset. The ratio L_{lig}/L_{Ag} here emerges as 1.30 ± 0.07.

Fig. 6 b shows the ligament size during the secondary dealloying at different ϕ as a function of t. Independent of ϕ, the L_{lig} data coincide. Moreover, at large t the graph converges to the growth law $L_{lig} \propto t^{1/4}$. This is expected for curvature-driven coarsening by surface diffusion [42] and has been confirmed in previous kMC studies of NPG coarsening [18]. We emphasize that Fig. 6b shows the identical $L_{lig}(t)$ dominating the coarsening during the entire period of the secondary dealloying. For the example of $\phi = 1.05$ eV, that period ranged from 10^4 s to about 10^6 s. This amounts to 99% of the whole dealloying time. While being decisive in determining structural sizes in the primary dealloying, the applied potential has – within the assumptions of our simulation – little influence on the growth kinetics during the secondary stage.

We now look at the relation between ligament size and residual silver content during the secondary stage. The log-log plot of Fig. 6c shows x_{Ag} versus L_{lig} for simulations with different ϕ. The essentially linear variation suggests the power law

$$L_{lig} \propto (x_{Ag})^m. \tag{4}$$

As shown in the inset of Fig 6c, straight-line fits to the data indicate that the exponent m is sensibly independent of the applied potential, $m = -0.57 \pm 0.02$.

4. Discussion

4.1. Two-stage characteristic of dealloying

The results of our simulations consolidate the notion [19] that the dealloying process comprises two clearly distinct stages, namely primary and secondary dealloying. During the primary stage, most of the less noble atoms are dissolved and a 3D network is formed. That process establishes lower limits of the ligament size which may be reached by dealloying, and it forms the initial topology of the ligament network [19,30]. The secondary dealloying stage is characterized by coarsening of the network structure by surface diffusion. The less noble atoms that were retained after primary dealloying are here slowly dissolved as they are exposed at surfaces during the microstructure evolution. In experiments, the two stages typically take place *concurrently*: While the corrosion front of primary dealloying progresses into the depth, secondary dealloying proceeds in its wake.

In corrosion experiments on macroscopic samples, primary and secondary dealloying will – in separate regions of the sample – generally occur simultaneously at any moment in time. By contrast, the extremely small size of our sample results in the two processes being essentially separated on the time axis. The corrosion front with its primary dealloying process quickly sweeps through the simulation volume, and noticeable secondary dealloying sets in only much later. Therefore, we can here separately analyze and discuss primary and secondary dealloying.

4.2. Ligament size during primary dealloying

In our simulation, the ligament size is found to vary as $L^{-1} \propto (\phi - \phi_0)$ with $\phi_0 \approx 900$ meV. In principle, this law would be expected if ϕ_0 could be identified with the Nernst potential and if a Gibbs-Thompson type relation linked the surface curvature – which scales with L^{-1} – to the overpotential, $\eta = (\phi - \phi_0)/q_e$. It is tempting to adopt this notion, not the least because 900 meV rather precisely compensates the free energy of formation of the alloy crystal in our simulation.[1] The scaling between $1/L$ and η

---

[1] For our model, the formation energy – which is also the enthalpy since the lattice is rigid - corresponds to 6 bonds per atom at a bond energy of -150 meV, or a total of -900 meV. The entropy (vibrational as well as configurational contributions) of the rigid lattice is zero for the pure components. Furthermore, under the

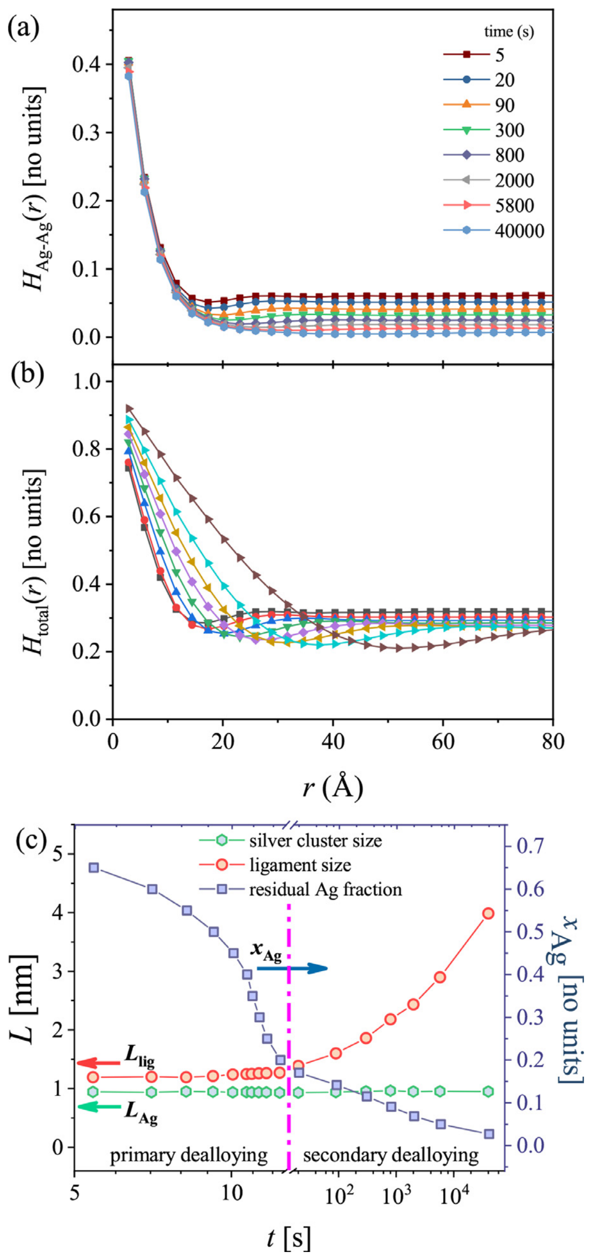

Fig. 5. Evolution of characteristic size during primary and secondary dealloying. (a) Ag-Ag correlation function, $H_{\text{Ag-Ag}}$, versus interatomic spacing r at different time. Note time-invariant initial slope. (b) Total correlation function, $H_{\text{total}}(r)$. Note that initial slopes decrease during secondary dealloying (time > 20 s). (c) Characteristic sizes of silver clusters (L_{Ag}) and of ligaments (L_{lig}) as determined from the initial slopes of the $H(r)$. Note constant L_{Ag} while L_{lig} increases during secondary dealloying. Ag fraction, x_{Ag}, is also shown. Bin size of 0.2885nm was used in constructing the $H(r)$. Overpotential is $\phi = 1.15$ eV.

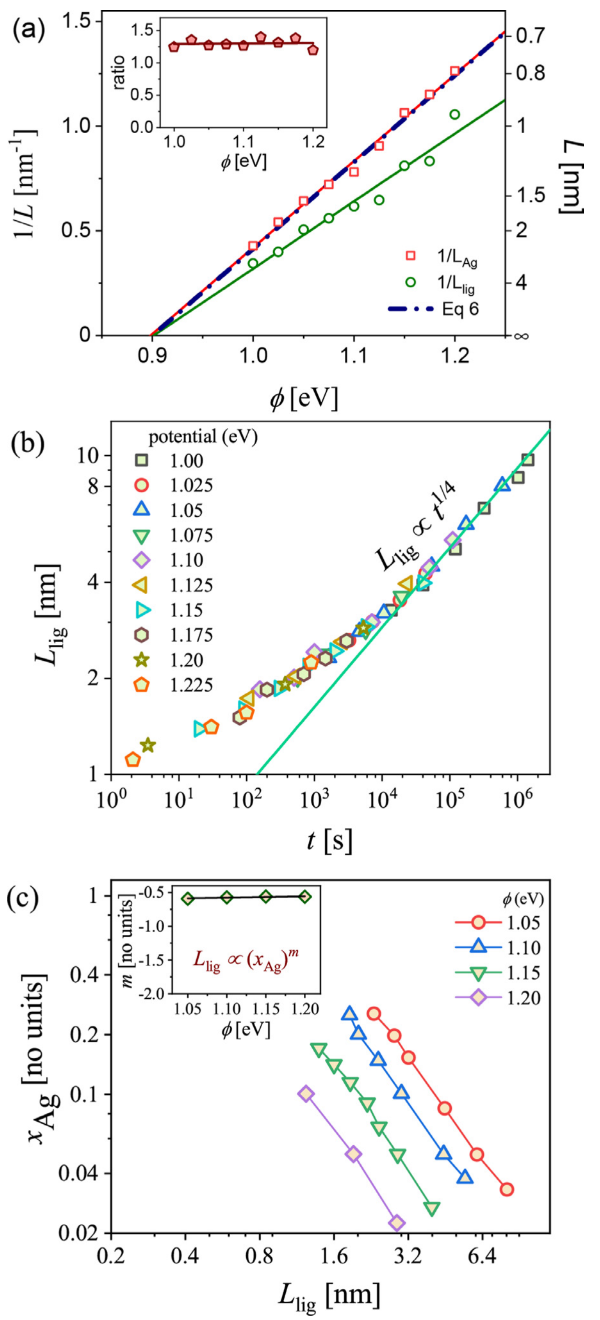

Fig. 6. Analysis of characteristic size. (a) Inverse of Ag cluster size, L_{Ag}, and of ligament size, L_{lig}, during primary dealloying versus dealloying potential, ϕ. Thin solid lines: linear regression. Note close agreement in abscissa intercepts at $\phi = 0.900 \pm 0.002$ eV. Bold dash-dotted line: Eq 6, using fit to data for abscissa intercept and the simulation's materials parameters for the slope. Agreement between predicted slope and data for L_{Ag} implies that Eq 6 underestimates data for L_{lig} by about 30 %. Inset shows ratio between the two characteristic sizes at each ϕ; horizontal line in inset denotes average value, 1.30 ± 0.07. (b) Log-log graph of L_{lig} during secondary dealloying versus time, t, for different ϕ. Note sensibly identical scaling behavior and trend towards $L \propto t^{1/4}$ at long time. (c) Log-log graph of Ag fraction, x_{Ag} vs. L_{lig}, during secondary dealloying. Apparent power law exponent was determined from straight lines of best fit and is plotted versus ϕ in insert.

would then be the inverse – namely generation of ever smaller structures with increasing overpotential – of the Gibbs-Thompson relation's trend for ever faster dissolution at smaller size and large overpotential. The appearance of an inverse behavior relates to the sign of the curvature: the convex particles (positive curvature) in a classic coarsening scenario have a stronger tendency for dissolution at smaller size. By contrast, the active ends of advancing pore channels in dealloying are concave (negative curvature). Thus, porosity evolution requires a stronger driving force for dissolution at smaller size [43,44]. A similar scenario in the context of dealloying has been discussed as an "inverse Gibbs-Thomson effect" [32],

---

conditions of our simulation, the dissolution events of Eq 2 are considerably more frequent than the diffusion jumps of Eq 1. The solid solution's configuration space is then not ergodically sampled within the brief timescale between a Ag atom being exposed to the mobile surface layer and the atom's dissolution. Therefore, the processes under investigation are not expected to be significantly affected by master-alloy entropy of mixing contributions.

and an inverse scaling between η and the length scale of alloy dissolution has been experimentally confirmed [45].

It is well established that the microstructure evolution during dealloying is governed by a competition between the trends for smoothening the surface corrugation and for passivation, both carried by surface diffusion, and a trend for new channels to propagate into the pristine master alloy below the surface, carried by dissolution [30,44,46]. In this sense it is not expected that an individual concept – such as the link between overpotential and curvature that is embodied in the Gibbs-Thompson relation – can, on its own, provide valid predictions for the microstructure evolution. Yet, the last-mentioned relation does provide a lower limit for the pore channel diameter that can be reached at any given value of η. We find it instructive to compare this lower limit to our observations.

Consider a cylindrical pore channel of diameter L, ending in a hemispherical cup (mean curvature $\kappa = -4/L$) that is the site of active corrosion. The minimum required overpotential is [44]

$$\eta = \frac{\gamma \Omega \kappa}{q_e} = \frac{4\gamma\Omega}{L q_e}, \tag{5}$$

where γ, Ω and q_e denote the specific surface excess free energy (or surface tension), atomic volume and elementary charge, respectively. Based on the excess energy in the broken bonds per area of surface, we find that our values of E_b and a imply $\gamma = 0.50$, 0.58, and 0.62 J/m^2, respectively, for {111}, {100}, and {110} terraces. As a rough estimate for a rough surface, we here use the mean of those values and work with $\gamma = 0.57$ J/m^2.

Solving Eq 5 for L and noting that $\phi = \phi_0 + \eta q_e$ we find a lower limit, $L_{\min}$, for the pore size at

$$L_{\min} = \frac{4\gamma\Omega}{\phi - \phi_0}. \tag{6}$$

The bold dash-dotted line in Fig 6 shows the prediction of Eq 6 in a representation of L^{-1} versus ϕ. We have used the empirical ϕ_0= 900 meV of the simulation results, yet we computed the slope by Eq 6 with the simulation's input values for Ω and γ. It is seen that the slope from Eq 6 coincides quite precisely with the data for the silver cluster size. The agreement with the data for the ligament size, which is the relevant quantity here, is less precise – by comparing the slopes, it is found that Eq 6 underestimates the ligament size by about the factor of 1.3. This may still count as a remarkable agreement, specifically when it is recalled that the equation presents a lower limit for the pore size. Note that pore and ligament sizes are expected reasonably similar in nanoporous metals with not too small φ. The qualitative agreement between data and theory supports the notion that the capillary terms of the Gibbs-Thompson relation are decisive for the link between ligament size and dealloying potential.

The aforementioned arguments also appear to support $\phi_0 =$ 900 meV as an estimate for the Nernst potential in our study. In the limit of $\phi \to \phi_0$, the dissolution could then provide less and less excess energy for creating surfaces, bulk dealloying would no longer be supported, and a critical dealloying potential, ϕ_c, would need to intervene at some value above ϕ_0. The expectation is indeed borne out as, for $Ag_{75}Au_{25}$, the model's ϕ_c is found between 900 and 950 meV [30]. Nonetheless, our simulation offers no conclusive support for such a scenario. Since re-deposition of silver atoms is ignored in the algorithm, the equilibrium between dissolution and redeposition through the exchange current–that is, the very process that defines the Nernst potential–cannot be modeled. All discussion of phenomena related to the overpotential must therefore be qualified as speculative here.

4.3. Ag cluster size during primary dealloying stage

As pointed out in this paper's introduction, dealloying has important applications as a process to forming nanomaterials with an extremely small microstructure. It is therefore of interest to investigate how the ligament size depends on the dealloying conditions. Specifically, the primary dealloying determines the lower limits of that size. Yet, the simultaneous action of primary and secondary dealloying in typical experiments makes the experimental isolation of the primary-dealloying ligament size challenging. In the previous section, we discussed the variation of the primary dealloying ligament size with the dealloying potential. Here, we explore how the above-mentioned challenge can be met.

While discussing the absolute value of L is challenging, the ratio $L^0_{\mathrm{lig}}/L_{\mathrm{Ag}}$ is more accessible to rationalization. That ratio can be simply understood as a consequence of the leftover more noble element being redistributed as a passivating layer on the pore surfaces. As long as the microstructure remains sensibly self-similar, the relative amounts of leftover more noble element and of residual pristine master alloy remain also sensibly similar. This translates into self-similar product structures where the thickness of the passivating layer scales with the size of the ligaments. Our observation on this scaling, namely $L^0_{\mathrm{lig}}/L_{\mathrm{Ag}} = 1.3$ irrespective of the absolute value of the primary dealloying ligament size, is important. This finding suggests that L^0_{lig} can be inferred from measurements of L_{Ag}. Since our results also show that this latter quantity does not vary during coarsening, postmortem investigations of the size of the Ag clusters in dealloyed NPG may be used to identify the ligament size during primary dealloying. Studies by TEM [26,33] and by atom-probe tomography [35] have shown that the cluster size is indeed accessible to experiment.

In studies of dealloying, the notion of cluster size arises also in a different context. The parting limit, that is, the minimum fraction of less noble element required for bulk dealloying, is inherently related to a percolation threshold – bulk dealloying requires a percolating cluster of less-noble element spanning the macroscopic volume of the solid solution [47–49]. Near the parting limit, the lateral extension of the individual percolating clusters – in a high-density-site percolation scenario – may be linked to the ligament size [45,50]. In our study, x_{Ag} of the starting alloy was substantially above the parting limit. The silver in the starting alloy may then form sensibly a single, extended cluster, as indeed exemplified by Fig 3a. The characteristic structure size after primary dealloying can then not be governed by the percolating silver cluster size in the starting alloy. Instead, the competition between passivation and corrosion and instabilities of the advancing corrosion front will be relevant [15,30], and the energy balance that is embodied in Gibbs-Thompson-type relations such as Eq 6 will impose a lower limit for the characteristic length scale.

4.4. Ligament coarsening during the secondary dealloying stage

Asymptotically at large time, we observe the evolution of the ligament size during secondary dealloying to follow the power law scaling, $L \propto t^{1/4}$, that has been observed in previous studies by kinetic Monte Carlo simulation [18]. While experiments do not agree on a time exponent for coarsening of NPG [51–53], the $t^{1/4}$ law is consistent with the established theory of surface-diffusion mediated, curvature-driven coarsening [42].

Our model does not link the surface diffusion to the dealloying potential. Not surprisingly, therefore, the coarsening emerges as independent of ϕ. We note that the experimental situation may be different, since the applied potential may substantially influence the surface diffusion coefficient [54,55] and, thereby, the coarsening rate [19].

4.5. Ag cluster size during secondary dealloying stage

Our analysis of the evolution of the characteristic length scales shows that the silver-rich clusters retain their original size from primary dealloying, even though the ligaments – into which the clusters are embedded – coarsen. In this context it is important to recall that the equilibrium vacancy concentration and the bulk diffusivity in gold at room temperature are exceedingly small [19,56,57]. That latter observation is implemented in our simulation code, which does not allow for bulk diffusion. Thus, the configuration of the silver clusters is frozen – and their size a constant – as long as they remain embedded in the bulk of the ligaments. As ligaments coarsen, the redistribution of gold by surface diffusion lets the surface migrate through the reference frame provided by the lattice sites. Whenever the surface intersects a cluster, corrosion acts to remove its silver. The cluster will then rapidly shrink and vanish.

5. Summary

Using kinetic Monte Carlo simulation, we studied the formation and evolution of the microstructure during the formation of nanoporous gold by electrochemical dealloying of Ag-Au. In the focus of the study are Ag-rich clusters and their relation to the ligament size in the earlier stages of corrosion. For comparability with previous studies, we adopted the model and its materials parameters from the earlier work. The results may be summarized as follows:

- As advertised in earlier work, dealloying is essentially a two-stage process. The network structure is formed during primary dealloying, and the subsequent secondary dealloying coarsens the network.
- The mean ligament size, L_{lig}^{0}, after primary dealloying decreases with increasing dealloying potential.
- As remnants of the master alloy, the as-dealloyed network contains Ag-rich clusters; their mean size, L_{Ag}, scales with L_{lig}^{0}.
- L_{lig} increases in the secondary dealloying stage. Ligament growth eventually converges to the classic power-law, $L_{\mathrm{lig}} \propto t^{1/4}$.
- Throughout the microstructure evolution–during both primary and secondary dealloying–L_{Ag} remains constant.

The finding that L_{Ag} scales with L_{lig}^{0} and remains constant during secondary dealloying has an important implication: Information on L_{lig}^{0}, as a crucial characteristic which has been challenging to access by experiment, can be reliably obtained by investigating the silver cluster size. Since that size is stable, the approach remains applicable even for samples that have undergone substantial coarsening during secondary dealloying.

We found $1/L_{\mathrm{lig}}^{0} \propto (\phi - \phi_0)$. In principle, this is consistent with a Gibbs-Thompson type relation between the overpotential and the maximum attainable local curvature at the tip of propagating pore channels. It would indeed be desirable to establish a link between overpotential and dealloying structure size. Yet, we emphasize that the present observations on their own provide no firm basis for clarifying the nature of this link. This is because the established kinetic Monte Carlo approach to dealloying – which also underlies our study – does not afford a reliable discussion of the Nernst potential or, in other words, of the absolute value of the overpotential. That advertises the interest in an expanded kinetic Monte Carlo model, implementing Ag redeposition on top of dissolution. Futures studies along those lines might afford quantifying the Nernst potential value that is consistent with the simulation scenario.

Declaration of Competing Interest

The authors whose names are listed immediately below certify that they have NO affiliations with or involvement in any organization or entity with any financial interest (such as honoraria; educational grants; participation in speakers' bureaus; membership, employment, consultancies, stock ownership, or other equity interest; and expert testimony or patent-licensing arrangements), or non-financial interest (such as personal or professional relationships, affiliations, knowledge or beliefs) in the subject matter or materials discussed in this manuscript.

Acknowlgedgments

This work was supported by the German Research Foundation (DFG) through grant WE1424/17-2, which is Subproject 3 within the Research Unit FOR2213 "NAGOCAT".

References

[1] D. Kramer, R.N. Viswanath, J. Weissmüller, Surface-stress induced macroscopic bending of nanoporous gold cantilevers, Nano Lett. 4 (5) (2004) 793–796.

[2] H.-J. Jin, X.-L. Wang, S. Parida, K. Wang, M. Seo, J. Weissmüller, Nanoporous au- pt alloys as large strain electrochemical actuators, Nano Lett. 10 (1) (2010) 187–194.

[3] E. Detsi, Z. Chen, W. Vellinga, P. Onck, J.T.M. De Hosson, Actuating and sensing properties of nanoporous gold, J. Nanosci. Nanotechnol. 12 (6) (2012) 4951–4955.

[4] X.-L. Ye, H.J. Jin, Sealing-free fast-response paraffin/nanoporous gold hybrid actuator, Nanotechnology 28 (38) (2017) 385501.

[5] S. Shi, J. Markmann, J. Weissmüller, Actuation by hydrogen electrosorption in hierarchical nanoporous palladium, Philos. Mag. 97 (19) (2017) 1571–1587.

[6] C. Xu, J. Su, X. Xu, P. Liu, H. Zhao, F. Tian, Y. Ding, Low temperature co oxidation over unsupported nanoporous gold, J. Am. Chem. Soc. 129 (1) (2007) 42–43.

[7] Y. Ding, M.W. Chen, Nanoporous metals for catalytic and optical applications, MRS Bull. 34 (2009) 569–576.

[8] A. Wittstock, V. Zielasek, J. Biener, C. Friend, M. Bäumer, Nanoporous gold catalysts for selective gas-phase oxidative coupling of methanol at low temperature, Science 327 (5963) (2010) 319–322.

[9] H. Qiu, L. Xue, G. Ji, G. Zhou, X. Huang, Y. Qu, P. Gao, Enzyme-modified nanoporous gold-based electrochemical biosensors, Biosens. Bioelectron. 24 (10) (2009) 3014–3018.

[10] C. Stenner, L.-H. Shao, N. Mameka, J. Weissmüller, Piezoelectric gold: strong charge-load response in a metal-based hybrid nanomaterial, Adv Funct Mater 26 (28) (2016) 5174–5181.

[11] E. Şeker, W.-C. Shih, K.J. Stine, Nanoporous metals by alloy corrosion: bioanalytical and biomedical applications, MRS Bull. 43 (1) (2018) 49–56.

[12] X. Lang, A. Hirata, T. Fujita, M. Chen, Nanoporous metal/oxide hybrid electrodes for electrochemical supercapacitors, Nat Nanotechnol 6 (4) (2011) 232–236.

[13] Y. Yu, L. Gu, X. Lang, C. Zhu, T. Fujita, M. Chen, J. Maier, Li storage in 3d nanoporous au-supported nanocrystalline tin, Adv. Mater. 23 (21) (2011) 2443–2447.

[14] Q. Chen, Y. Ding, M. Chen, Nanoporous metal by dealloying for electrochemical energy conversion and storage, MRS Bull. 43 (1) (2018) 43–48.

[15] J. Erlebacher, M.J. Aziz, A. Karma, N. Dimitrov, K. Sieradzki, Evolution of nanoporosity in dealloying, Nature 410 (6827) (2001) 450–453.

[16] D.A. Crowson, D. Farkas, S.G. Corcoran, Mechanical stability of nanoporous metals with small ligament sizes, Scr Mater 61 (5) (2009) 497–499.

[17] H.-J. Jin, L. Kurmanaeva, J. Schmauch, H. Rösner, Y. Ivanisenko, J. Weissmüller, Deforming nanoporous metal: role of lattice coherency, Acta Mater 57 (9) (2009) 2665–2672.

[18] Y. Li, B.-N.D. Ngô, J. Markmann, J. Weissmüller, Topology evolution during coarsening of nanoscale metal network structures, Physical review materials 3 (7) (2019) 076001.

[19] X.-L. Ye, N. Lu, X.-J. Li, K. Du, J. Tan, H.J. Jin, Primary and secondary dealloying of au (pt)-ag: structural and compositional evolutions, and volume shrinkage, J Electrochem Soc 161 (12) (2014) C517.

[20] M. Graf, B. Roschning, J. Weissmüller, Nanoporous gold by alloy corrosion: method-structure-property relationships, J Electrochem Soc 164 (4) (2017) C194–C200.

[21] A. Hodge, R. Doucette, M. Biener, J. Biener, O. Cervantes, A. Hamza, Ag effects on the elastic modulus values of nanoporous au foams, J Mater Res 24 (4) (2009) 1600–1606.

[22] N. Beets, D. Farkas, K. Albe, The mechanical response of nanoporous gold and silver foams with varying composition and surface segregation, Acta Mater 203 (2020) 116445.

[23] L. Zhang, L. Chen, H. Liu, Y. Hou, A. Hirata, T. Fujita, M. Chen, Effect of residual silver on surface-enhanced raman scattering of dealloyed nanoporous gold, The Journal of Physical Chemistry C 115 (40) (2011) 19583–19587.

[24] L. Wang, Y. Zhong, D. Widmann, J. Weissmüller, R. Behm, On the role of residual ag in nanoporous au catalysts for co oxidation: a combined microreactor and tap reactor study, ChemCatChem 4 (2) (2012) 251–259.
[25] A. Wittstock, M. Bäumer, Catalysis by unsupported skeletal gold catalysts, Acc. Chem. Res. 47 (3) (2014) 731–739.
[26] C. Mahr, P. Kundu, A. Lackmann, D. Zanaga, K. Thiel, M. Schowalter, M. Schwan, S. Bals, A. Wittstock, A. Rosenauer, Quantitative determination of residual silver distribution in nanoporous gold and its influence on structure and catalytic performance, J Catal 352 (2017) 52–58.
[27] A. Lackmann, M. Bäumer, G. Wittstock, A. Wittstock, Independent control over residual silver content of nanoporous gold by galvanodynamically controlled dealloying, Nanoscale 10 (36) (2018) 17166–17173.
[28] Z. Qi, J. Weissmüller, Hierarchical nested-network nanostructure by dealloying, ACS Nano 7 (7) (2013) 5948–5954.
[29] S. Shi, Y. Li, B.-N. Ngo-Dinh, J. Markmann, J. Weissmüller, Scaling behavior of stiffness and strength of hierarchical network nanomaterials, Science 371 (6533) (2021) 1026.
[30] J. Erlebacher, An atomistic description of dealloying porosity evolution, the critical potential, and rate-limiting behavior, J Electrochem Soc 151 (10) (2004) C614–C626.
[31] J. Erlebacher, Mechanism of coarsening and bubble formation in high-genus nanoporous metals, Phys. Rev. Lett. 106 (22) (2011) 225504.
[32] I.M. Cue, J. Snyder, X. Li, Q. Chen, K. Sieradzki, J. Erlebacher, Apparent inverse gibbs-thomson effect in dealloyed nanoporous nanoparticles, Phys. Rev. Lett. 108 (22) (2012).
[33] T. Krekeler, A.V. Straßer, M. Graf, K. Wang, C. Hartig, M. Ritter, J. Weissmüller, Silver-rich clusters in nanoporous gold, Materials Research Letters 5 (5) (2017) 314–321.
[34] P. Haldar, A. Chatterjee, Extent of dissolution determines the structural similarity between dealloyed nanoporous materials synthesized at unrelated dissolution conditions, Acta Mater 152 (2018) 186–198.
[35] A.A. El-Zoka, B. Langelier, G.A. Botton, R.C. Newman, Enhanced analysis of nanoporous gold by atom probe tomography, Mater Charact 128 (2017) 269–277.
[36] C.J. Dotzler, B. Ingham, B.N. Illy, K. Wallwork, M.P. Ryan, M.F. Toney, In situ observation of strain development and porosity evolution in nanoporous gold foils, Adv Funct Mater 21 (20) (2011) 3938–3946.
[37] B. Lin, L. Kong, P.D. Hodgson, S. Mudie, A. Hawley, L.F. Dumée, Controlled porosity and pore size of nano-porous gold by thermally assisted chemical dealloying–a saxs study, RSC Adv 7 (18) (2017) 10821–10830.
[38] E.J. Schofield, B. Ingham, A. Turnbull, M.F. Toney, M.P. Ryan, Strain development in nanoporous metallic foils formed by dealloying, Appl Phys Lett 92 (4) (2008) 043118.
[39] A. Stukowski, Visualization and analysis of atomistic simulation data with ovito–the open visualization tool, Modell. Simul. Mater. Sci. Eng. 18 (1) (2009) 015012.
[40] P. Debye, H. Anderson Jr., H. Brumberger, Scattering by an inhomogeneous solid. ii. the correlation function and its application, J Appl Phys 28 (6) (1957) 679–683.
[41] J. Löffler, J. Weissmüller, Grain-boundary atomic structure in nanocrystalline palladium from x-ray atomic distribution functions, Physical review B 52 (10) (1995) 7076.
[42] C. Herring, Effect of change of scale on sintering phenomena, J Appl Phys 21 (4) (1950) 301–303.
[43] K. Sieradzki, Curvature effects in alloy dissolution, J Electrochem Soc 140 (10) (1993) 2868–2872.
[44] K. Sieradzki, N. Dimitrov, D. Movrin, C.M. Call, N. Vasiljevic, J. Erlebacher, The dealloying critical potential, J Electrochem Soc 149 (8) (2002) B370–B377.
[45] J. Rugolo, J. Erlebacher, K. Sieradzki, Length scales in alloy dissolution and measurement of absolute interfacial free energy, Nat Mater 5 (12) (2006) 946–949.
[46] J. Weissmüller, R.C. Newman, H.J. Jin, A.M. Hodge, J.W. Kysar, Nanoporous metals by alloy corrosion: formation and mechanical properties, MRS Bull. 34 (8) (2009) 577–586.
[47] K. Sieradzki, R.C. Newman, Stress-corrosion cracking, J. Phys. Chem. Solids 48 (11) (1987) 1101–1113.
[48] K. Sieradzki, R.R. Corderman, K. Shukla, R.C. Newman, Computer simulations of corrosion: selective dissolution of binary alloys, Philos. Mag. A 59 (4) (1989) 713–746.
[49] Q. Chen, K. Sieradzki, Mechanisms and morphology evolution in dealloying, J Electrochem Soc 160 (6) (2013) C226–C231.
[50] D. Artymowicz, J. Erlebacher, R. Newman, Relationship between the parting limit for de-alloying and a particular geometric high-density site percolation threshold, Philos. Mag. 89 (21) (2009) 1663–1693.
[51] L. Qian, M. Chen, Ultrafine nanoporous gold by low-temperature dealloying and kinetics of nanopore formation, Appl Phys Lett 91 (8) (2007) 083105.
[52] Y.-c.K. Chen-Wiegart, S. Wang, Y.S. Chu, W. Liu, I.M. Nulty, P.W. Voorhees, D.C. Dunand, Structural evolution of nanoporous gold during thermal coarsening, Acta Mater 60 (12) (2012) 4972–4981.
[53] S. Kuwano-Nakatani, T. Fujita, K. Uchisawa, D. Umetsu, Y. Kase, Y. Kowata, K. Chiba, T. Tokunaga, S. Arai, Y. Yamamoto, et al., Environment-sensitive thermal coarsening of nanoporous gold, Materials Transactions 56 (4) (2015) 468–472.
[54] J.M. Dona, J. Gonzalez-Velasco, The dependence of the surface-diffusion coefficients of gold atoms on the potential - its influence on reconstruction of metal lattices, Surf Sci 274 (2) (1992) 205–214.
[55] J.M. Dona, J. Gonzalez-Velasco, Mechanism of surface-diffusion of gold adatoms in contact with an electrolytic solution, J. Phys. Chem. 97 (18) (1993) 4714–4719.
[56] K. Dick, T. Dhanasekaran, Z. Zhang, D. Meisel, Size-dependent melting of silica-encapsulated gold nanoparticles, J. Am. Chem. Soc. 124 (10) (2002) 2312–2317.
[57] X. Li, Q. Chen, I.M. Cue, J. Snyder, P. Crozier, J. Erlebacher, K. Sieradzki, Dealloying of noble-metal alloy nanoparticles, Nano Lett. 14 (5) (2014) 2569–2577.